第 35 卷第 3 期
2019 年 3 月

无 机 化 学 学 报
CHINESE JOURNAL OF INORGANIC CHEMISTRY

Vol.35 No.3
553-562

# 低负载量的双金属 Au@Pt 核壳催化剂催化氧化甲苯

李思汉 李小青 胡凤腾 张 超 严新焕*

(浙江工业大学绿色化学合成技术国家重点实验室培育基地,杭州 310014)

**摘要**: 采用液相氢气两步还原法制备了双金属 Au@Pt 核壳纳米粒子,通过直接吸附法将纳米粒子均匀地分散于载体上,制备出低负载量的双金属 Au@Pt/$Al_2O_3$ 催化剂, 并且评价了催化剂对甲苯的催化氧化性能。通过 TEM、XRD、XPS、$N_2$ 吸附–脱附和 $H_2$-TPR 等对催化剂进行了表征。结果表明,与单金属 Au 和 Pt 催化剂相比,双金属 Au@Pt 核壳催化剂表现出更高的催化活性,具有很好的稳定性和选择性,在甲苯体积分数为 $1\times10^{-3}$,气体空速为 18 $L\cdot g^{-1}\cdot h^{-1}$ 的条件下,$Au_1@Pt_2/Al_2O_3$ 核壳催化剂具有优异的催化氧化性能,其中甲苯实现 98%的转化率的温度($T_{98}$)为 195 ℃。由 XPS 结果可知,在 Au 和 Pt 之间存在电子转移促进了 Pt 上活性氧物种的形成,催化剂的活性组分主要以 $Au^0$ 和 $Pt^0$ 的形式存在,并广泛分布在载体的表面上。Au@Pt 纳米粒子与载体 $Al_2O_3$ 之间的强相互作用也是提高甲苯催化氧化活性的重要因素。

**关键词**: 双金属; Au@Pt; 核壳; 挥发性有机物; 甲苯; 催化氧化

**中图分类号**: O614.123; O614.82+6; TB331 **文献标识码**: A **文章编号**: 1001-4861(2019)03-0553-10

**DOI**: 10.11862/CJIC.2019.055

## Catalytic Oxidation of Toluene with Low Loading Bimetallic Au@Pt Core-Shell Catalyst

LI Si-Han LI Xiao-Qing HU Feng-Teng ZHANG Chao YAN Xin-Huan*

(*State Key Laboratory Breeding Base of Green Chemistry-Synthesis Technology, Zhejiang University of Technology, Hangzhou* 310014, *China*)

**Abstract:** Highly active bimetallic Au@Pt core-shell catalysts were prepared by using direct-adsorption method, in which uniformly dispersed Au@Pt nanoparticles synthesized using two-step liquid-phase hydrogen reduction method were directly loaded on support. The performance of the catalysts for catalytic oxidation of toluene was evaluated. The catalysts were characterized by transmission electron microscopy (TEM) in conjunction with energy dispersive spectroscopy (EDS), X-ray diffraction (XRD), X-ray photoelectron spectroscopy (XPS), $N_2$ adsorption-desorption and temperature-programmed reduction ($H_2$-TPR). As a result, the bimetallic Au@Pt core-shell catalysts exhibited higher catalytic activity compared with monometallic Au or Pt catalyst, and the $Au_1@Pt_2/Al_2O_3$ core-shell catalyst showed outstanding catalytic activity, selectivity and stability among the bimetallic catalysts. The temperature for conversion of 98% toluene ($T_{98}$) was 195 ℃ under the condition of toluene volume fraction at $1\times10^{-3}$ and the gas hourly space velocity of 18 $L\cdot g^{-1}\cdot h^{-1}$.The XPS results illustrated that the enhancement of catalytic activity is attributed to the presence of Au underneath Pt shell where electron exchange from Au to Pt has promoted the formation of active oxygen species on Pt, which facilitates the oxidation of toluene. In addition, the active components of the catalyst mainly existed in the form of $Au^0$ and $Pt^0$, and the strong interaction between the Au@Pt nanoparticles and the support was observed.

**Keywords:** bimetallic; Au@Pt; core-shell; VOCs; toluene; catalytic oxidation

收稿日期:2018-10-11。收修改稿日期:2018-12-10。

国家重点研发计划(No.2017YFC0210900)和浙江省科技计划项目(No.2016C31104)资助。

*通信联系人。E-mail:xhyan@zjut.edu.cn

## 0 Introduction

Volatile organic compounds (VOCs) are the major component of environmental pollution from a larger variety of sources, such as transport, industrial process and household products[1-3]. VOCs are also important precursors for the formation of particulate matter (PM), ozone and photochemical smog, which greatly threaten to the environment and human health due to their toxic, mutagenic and teratogenic characteristics[4-6]. The development of efficient and low-energy methods for removing VOCs is one of the important means to ease the world′s energy and environmental problems. Until now, the main approaches[7] for removing VOCs include adsorption, absorption, photocatalysis, biodegradation, pulse corona, catalytic oxidation, etc. Among these methods, catalytic oxidation is considered to be one of the most effective and commonly used methods for eliminating VOCs, which can remove VOCs with low energy consumption, no secondary pollution is found as only $CO_2$ and $H_2O$.

Currently, gold nanoparticles (NPs) have traditionally been utilized as catalytically active centers for noble metal deposition to prepare bimetallic core-shell structures. Among the various noble metals, bimetallic Au@Pt core-shell nanoparticles are considered a typical example and have been extensively studied and used, which can increase the activity, stability and selectivity in specific chemical reactions compared to monometallic Pt or Au. The improvement of performance is attributed to the synergy of the electronic and geometric effects between the two metals[8]. In addition, the bimetallic Au@Pt core-shell also can reduce the amount of Pt loading and improve the utilization of Pt compared with alloyed structures[9].

Recently, many approaches have been applied to synthesize Au@Pt core-shell nanoparticles including electrodeposition[10-11], chemical reduction[12-13] and galvanic displacement[14-15]. The procedures of electrodeposition and galvanic displacement are complicated and cumbersome. The reaction often occurs under the harsh conditions, such as the use of poisonous and stubborn surfactant agents, high temperature, strong acid and alkali solvents. On the basis of economic and environmental considerations, the preparation of core-shell nanoparticles by a simple method remains still a challenge.

Herein, we developed a new and environmentally friendly method for the preparation of Au@Pt core-shell nanoparticles: the Au nanoparticles were firstly prepared by liquid-phase hydrogen reduction, then small Pt particles were deposited onto the Au nanoparticles to obtain Au@Pt core-shell nanostructures. Compared with the conventional method, this method can effectively control the particle size and crystal structure. Moreover, it can regulate the dispersion of the active components on the carrier. The low loading Au@Pt core-shell catalyst showed higher activity for toluene oxidation at low temperature.

## 1 Experimental

### 1.1 Materials

$HAuCl_4 \cdot 4H_2O$ and $H_2PtCl_6 \cdot 6H_2O$ (AR) were purchased from Shanghai Tuosi Chemical Co., Ltd. Propylene carbonate (AR) was purchased from Dongguan Youte environmental protection materials Co., Ltd. $\gamma$-$Al_2O_3$ was purchased from Shanghai Lüqiang New Material Co., Ltd. Toluene (AR) was purchased from Aladdin.

### 1.2 Preparation of nanoparticles

1.2.1 Preparation of Au nanoparticles

Au nanoparticles were synthesized by using $HAuCl_4 \cdot 4H_2O$ as a precursor. The measured amount of $HAuCl_4 \cdot 4H_2O$ was sufficiently dissolved in 100 mL of propylene carbonate and added to the autoclave. The reaction was carried out at 40 ℃ under hydrogen pressure of 4 MPa for 2 h to obtain Au nanoparticles solution. $\gamma$-$Al_2O_3$ was added into the above solution, stirred for 24 h and calcined at 400 ℃ for 4 h after filtrating and drying. The combined catalyst with low Au loading 0.04% (mass fraction) was obtained and recorded as Au/$\gamma$-$Al_2O_3$.

1.2.2 Preparation of Au@Pt core-shell nanoparticles

The calculated amount ($n_{Au}$:$n_{Pt}$=1:0, 3:1, 2:1, 1:1, 1:2, 1:3, 0:1) of $H_2PtCl_6 \cdot 6H_2O$ was added in the above-prepared Au nanoparticles solution. Then the

mixed solution was added to the autoclave with 4 MPa $H_2$. The solution was vigorously stirred for 3 h at 40 ℃ to obtain Au@Pt core-shell nanoparticles. To deposit the sol on the support, a certain amount of the pretreated $\gamma$-$Al_2O_3$ carrier was added to the above nanoparticle solution. After stirring and impregnating 24 h, the sample was filtered, dried and then calcined in the muffle furnace at 400 ℃ for 4 h to obtain combined core-shell Au@Pt catalysts (the loading amount was shown in Table 1).

**Table 1　Metal loading determined by ICP-AES and physical property of prepared catalysts**

| Sample | Theoretical load[a] of Au/% (*w*/*w*) | Theoretical load[a] of Pt/% (*w*/*w*) | Actual load[b] of Au / % (*w*/*w*) | Actual load[b] of Pt / % (*w*/*w*) | Actual atomic ratio[b] | $S_{BET}$[c] / ($m^2 \cdot g^{-1}$) | $D_P$[d] / nm | $V_P$[e] / ($cm^3 \cdot g^{-1}$) |
|---|---|---|---|---|---|---|---|---|
| $Al_2O_3$ | — | — | — | — | — | 357 | 15.1 | 1.50 |
| $Au/Al_2O_3$ | 0.040 | 0 | 0.035 | 0 | Au | 322 | 11.9 | 1.10 |
| $Au_3Pt_1/Al_2O_3$ | 0.040 | 0.013 | 0.032 | 0.011 | $Au_{2.88}Pt_1$ | 331 | 12.8 | 1.12 |
| $Au_2Pt_1/Al_2O_3$ | 0.040 | 0.020 | 0.036 | 0.017 | $Au_{2.01}Pt_1$ | 333 | 13.0 | 1.20 |
| $Au_1Pt_1/Al_2O_3$ | 0.040 | 0.040 | 0.030 | 0.035 | $Au_{0.84}Pt_1$ | 338 | 13.7 | 1.14 |
| $Au_1Pt_2/Al_2O_3$ | 0.040 | 0.079 | 0.038 | 0.070 | $Au_{1.08}Pt_2$ | 342 | 14.7 | 1.26 |
| $Au_1Pt_3/Al_2O_3$ | 0.040 | 0.118 | 0.037 | 0.109 | $Au_{1.01}Pt_3$ | 341 | 14.5 | 1.24 |
| $Pt/Al_2O_3$ | 0 | 0.080 | 0 | 0.074 | Pt | 333 | 13.2 | 1.21 |

[a] Loading content of Pt and Au was calculated on the assumption that none loss of catalyst during the preparation process; [b] Determined by the ICP-AES technique; [c] specific surface area; [d] pore diameter; [e] pore volume.

### 1.3　Catalyst characterization

The XRD patterns of the materials were performed on a Rigaku D/Max-2500 X-ray diffractometer, which used a Cu $K\alpha$ radiation ($\lambda$=0.154 nm) in the $2\theta$ scan range (40 kV and 100 mA) from 10° to 80° with a step of 0.05°. Transmission electron microscopy (TEM) was taken on a JEOL JEM-1200EX with an accelerating voltage of 60 kV equipped with energy dispersive spectroscopy (EDS). The X-ray photoelectron spectrometer (XPS) was carried on non-monochromatic Al $K\alpha$ (1 486.6 eV) radiation. The $N_2$ adsorption-desorption experiments were measured at liquid nitrogen temperature (77 K). The specific surface area of the material was calculated from the desorption isotherm by Brunauer-Emmett-Teller (BET) theory. The different $H_2$ reduction temperature and hydrogen consumption of different oxidation state substances was measured using $H_2$-TPR (temperature programmed reduction) method with online thermal conductivity detector (TCD) recording the temperature dependence of $H_2$ concentration.

### 1.4　Catalytic activity measurements

The catalytic activity of the catalyst was evaluated in the self-made atmospheric fixed bed catalytic reaction device. The catalyst (0.5 g) was placed in the middle of the reaction tube. The saturated toluene vapor of 0 ℃ was introduced into the reaction tube by bubbling method. In the feed stream, the concentration (volume fraction) was $1\times10^{-3}$ and gas hourly space velocity (GHSV) of VOCs was 18 000~54 000 $mL \cdot g^{-1} \cdot h^{-1}$. The toluene and oxide content in the tail gas was monitored online by gas chromatography with a flame ionization detector (FID) and a TCD to determine toluene conversion and $CO_2$ selectivity at different temperatures, and the temperature at which toluene achieved 98% conversion was recorded as $T_{98}$.

The conversion of toluene and selectivity of $CO_2$ are calculated as follows:

$$C_7H_8 \text{ conversion}=\frac{\varphi_{C_7H_8,in}-\varphi_{C_7H_8,out}}{\varphi_{C_7H_8,in}}\times100\%$$

$$CO_2 \text{ selectivity}=\frac{\varphi_{CO_2}}{\varphi_{CO_2}+\varphi_{CO}}\times100\%$$

where $\varphi_{C_7H_8,in}$ and $\varphi_{C_7H_8,out}$ represent the volume fraction of toluene before and after reaction, respectively; $\varphi_{CO_2}$ and $\varphi_{CO}$ represent the volume fraction of $CO_2$ and CO.

## 2　Results and discussion

### 2.1　Catalyst load test

The metal loading of different Au-Pt molar ratio

catalysts were determined by ICP-AES (Table 1). It can be seen that the actual loading is slightly lower than the theoretical calculation, indicating that a loss of some metal might occur during the synthesis or calcination step. However, it has little influence on the catalyst within the margin of error, which can be neglected basically. Therefore, the actual atomic ratio of the catalyst can be replaced by the theoretical value.

## 2.2 Morphology and structure of the catalyst

Fig.1 shows the TEM images and particle size distributions of Au and Au-Pt nanoparticles. The monometallic Au nanoparticles were uniformly dispersed with wide particle size distribution in a range of 3.75 ~10.61 nm and the average size was 6.57 nm (Fig.1a). Due to the effect of propylene carbonate as dispersant and stabilizer, nanoparticles are directly adsorbed on the surface of the support,

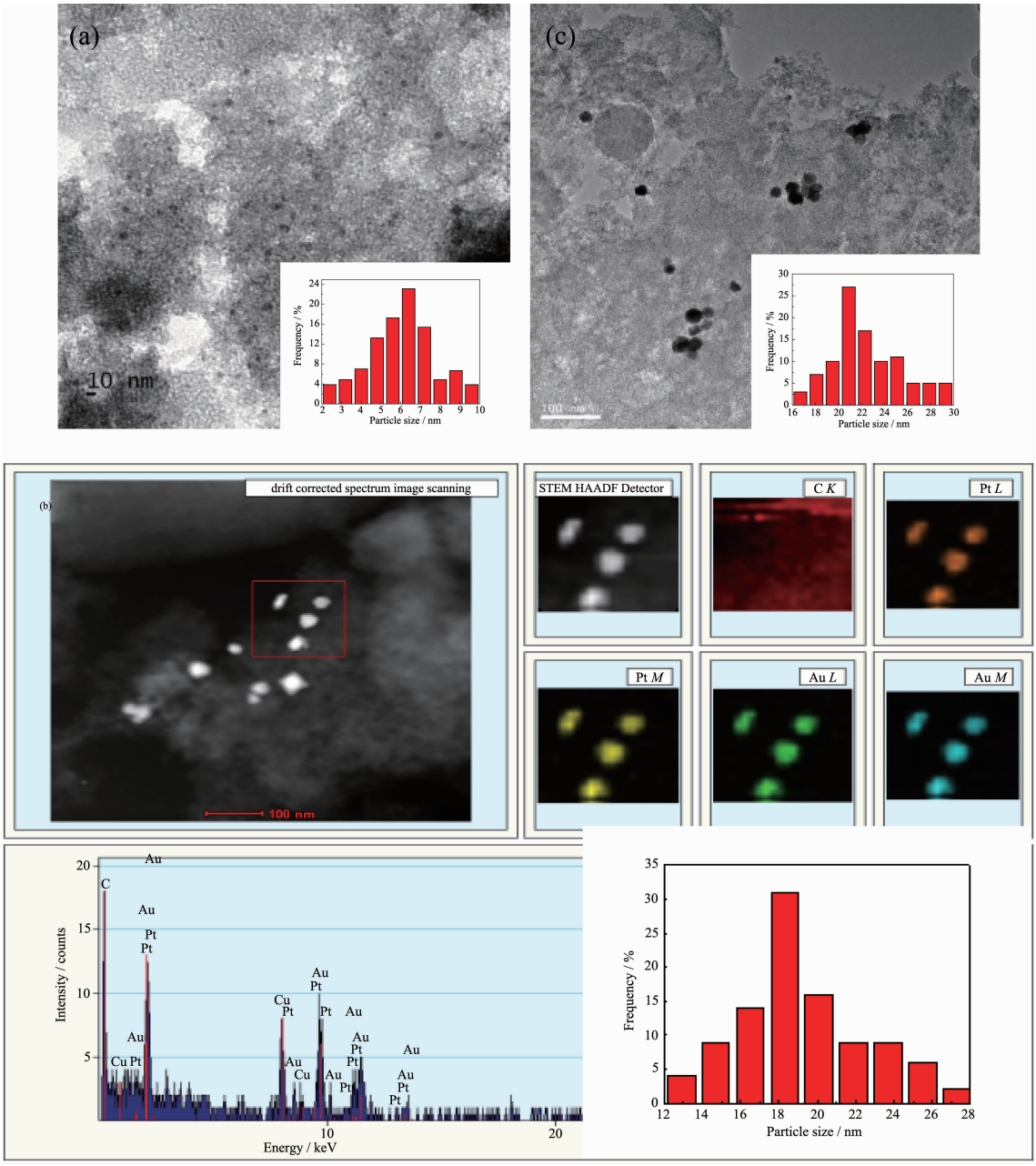


Fig.1 TEM image of Au nanoparticles (a), elemental mapping of bimetallic $Au_1Pt_2$ nanoparticles (b), TEM image of bimetallic $Au_1Pt_2$ nanoparticles after reaction (c) and the corresponding particle size distributions

which effectively inhibits the growth of nanoparticles and hinders the penetration of nanoparticles into the pores of the support[16]. Thus Au nanoparticles have smaller size of the active phase and finer dispersion. The bimetallic Au-Pt nanoparticles were significantly larger than the monometallic Au. The sizes (Fig.1b) were between 12.5 and 29.1 nm, and the average size was 18.3 nm. This indicates that Au nanoparticles gradually grow, which results from the deposition of Pt on the surface of Au or the agglomeration of Au(Pt) nanoparticles. As can be seen from Fig.1c, the catalyst after reaction showed partial agglomeration and the overall particle size increased, but the amplitude of variation was not significant, demonstrating that the catalyst remain stable and is consistent with XRD characterization. However, the TEM images of bimetallic Au-Pt do not allow us to distinguish between Au and Pt particles because Au and Pt exhibit almost the same imaging contrast and similar crystal structure[17]. From the elemental mapping images of bimetallic Au-Pt NPs (Fig.1b), Au-L (M) and Pt-L (M) which are represented by different colors corresponded to each other, that is, the regions with Au must have the presence of Pt. This indicates that Pt grows on the surface of Au instead of forming its own nucleus or that Au and Pt are physically mixed together, which may form core-shell or alloy structure.

High-resolution TEM (HRTEM) images of Au-Pt nanoparticles are shown in Fig.2. In order to verify the core-shell structure of nanoparticles, we performed Fourier transform on the high-resolution structures to obtain the corresponding diffraction patterns. The lattice spacing was calculated by using digital photomicrography software. From the diffraction pattern (Fig.2), the lattice spacing at the center position of the nanoparticles (1#) was 0.235 nm for the (111) lattice

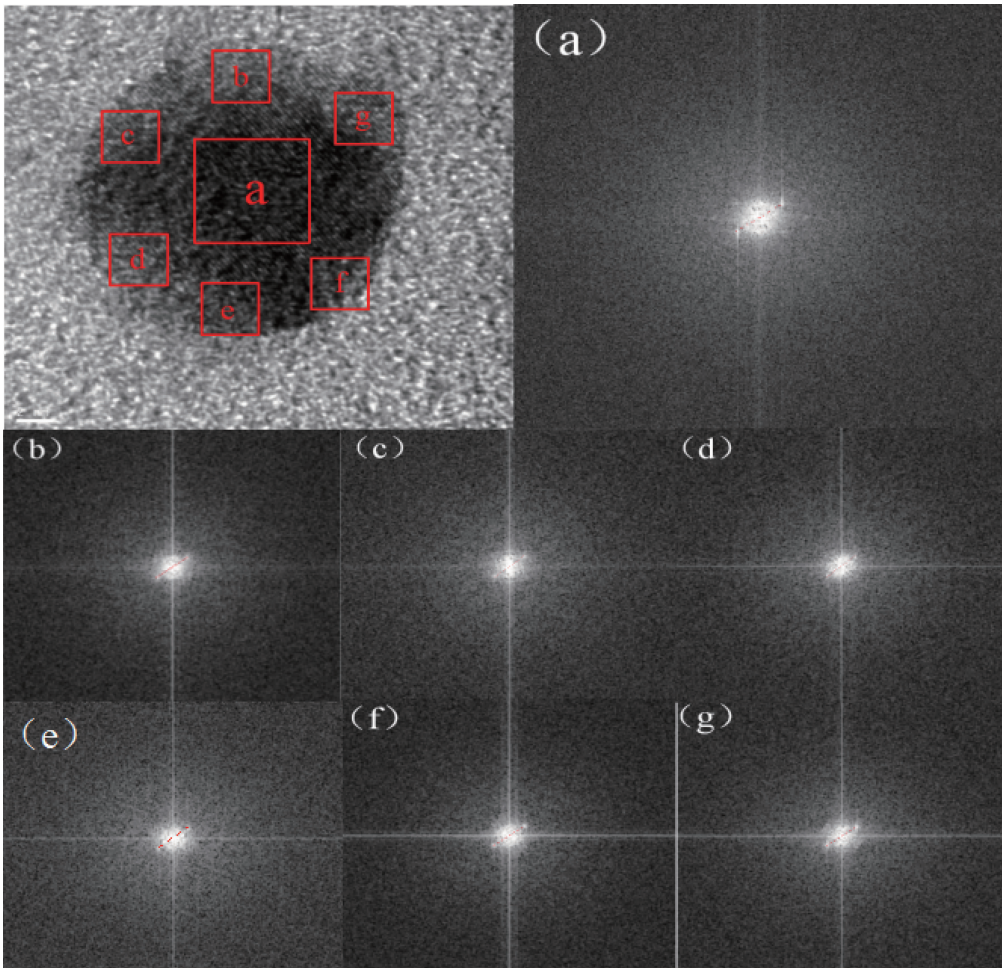


Fig.2　HRTEM image of Au-Pt nanoparticles corresponding to the first point in Fig.1b and FFT patterns of each area (a~g)

planes of *fcc* metallic Au[18]. The lattice spacing of the diffraction fringes in the b~g region (Fig.2) was 0.224, 0.225, 0.226, 0.225, 0.224 and 0.225 nm for the (111) lattice planes of *fcc* metallic Pt[19]. The HRTEM image of the Au-Pt nanoparticles revealed that the d-spacings of adjacent fringes for metal cores and metal surrounding were (0.235±0.002) nm and (0.225±0.002) nm[20], respectively, corresponding to the (111) planes of face-centered cubic Au and Pt, which indicates that bimetallic Au@Pt NPs are core/shell structures. In order to verify the universality of this conclusion, we selected two more points (Fig.S1 and S2), and the lattice spacings of a~g and b~g regions was shown in Table S1, which matches well with the (111) planes of the Au and Pt, respectively. We can draw the same conclusion that the nanoparticle must be core-shell structure, which accords with elemental mapping of Au@Pt nanoparticles.

The XRD patterns of $\gamma$-$Al_2O_3$, supported catalysts and the standard diffraction peaks of Au and Pt are shown in Fig.3. The diffraction pattern for monometallic Pt had several peaks at 39.8°, 46.2° and 67.4°, corresponding to (111), (200) and (220) planes (PDF No.89-7382), respectively. Wide-angle X-ray diffraction showed broad peaks at 38.2°, 44.4°, 64.6°, 77.5°, which are characteristic of (111), (200), (220) and (311) planes of monometallic Au (PDF No.89-3697), respectively. The XRD patterns of the bimetallic Au@Pt core-shell catalysts matched quite well with the (111), (200), (220) and (311) peaks in the Au pattern and no diffraction peaks of Pt can be observed. This indicates that only a monolayer of Pt is deposited on Au without forming individual Pt particles[21] or there exist small size Pt particles (1~2 nm, which can be undetected by XRD technique) or the loading of Pt on the Au surface is very low[22], otherwise the Au and Pt peaks of physical mixture would appear in the XRD pattern. From Fig.3, it can be seen that the XRD peak of Au (220) and (311) tended to be flat with the increase of Pt content in the bimetallic catalysts. The Au@Pt particle size on the support become smaller with increasing Pt content. Among the prepared Au@Pt/$\gamma$-$Al_2O_3$ catalyst, the maximum dispersion was obtained by $Au_1@Pt_2$ catalyst, which leads to high catalytic activity. As can be seen from the XRD pattern of $Au_1@Pt_2/\gamma$-$Al_2O_3$ catalyst after reaction, the number of diffraction peaks did not change and the structure did not change significantly, indicating that the catalyst has good stability.

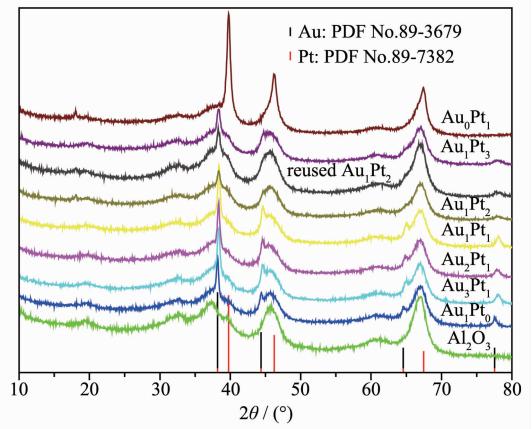


Fig.3 XRD patterns for Au@Pt NPs prepared with different molar ratios

## 2.3 Reducibility of catalyst

Table 1 shows the physical structure properties of the supported catalyst and support $\gamma$-$Al_2O_3$. Compared with support $\gamma$-$Al_2O_3$, the specific surface area, pore size and pore volume of the supported catalyst were reduced, which may be due to the blockage of $\gamma$-$Al_2O_3$ pores by some nanoparticles during the preparation process. However, the specific surface area and pore volume of $Au_1@Pt_2/\gamma$-$Al_2O_3$ were relatively larger than other catalysts. The $Au_1@Pt_2$ nanoparticles are mainly distributed on the surface of the support and have relatively less influence on the support structure. It is well known that the distribution of active components is one of the most important factors to affect the activity of the catalyst, especially for the gas-solid reactions. The more active components are located on the surface of the support, the more effective active sites are provided for the reaction. What′s more, the time for the reactant to enter the inner pore and the product to diffuse out from the inner pores is shortened, thereby greatly improving the activity of the catalyst[23].

It is known to all that the reducibility of catalysts can play an important role in the redox reactions. For

metal oxide catalysts, $H_2$-TPR measurement can reflect the reduction of high-valent metal ions to low-valent metal ions or metal-atom, as well as the potential to remove or absorb oxygen[24]. The $H_2$-TPR profiles of Au@Pt catalysts are shown in Fig.4. For $Au/Al_2O_3$, there were two reduction peaks. The first weak peak around 324 ℃ is attributed to the reduction of $Au_xO_y$[25], which coincides with the results of XRD with the presence of oxides. And the second peak obtained at 598 ℃ can correspond to the reduction of gold ions ($Au^+$) in the subsurface of support[26]. For $Pt/Al_2O_3$, the first peak at 93 ℃ can be assigned to the reduction of $PtO_x$, which contains the contribution of the surface oxygen adjacent to Pt species due to the spillover effect induced by the metal-support interaction. The second peak at 502 ℃ is ascribed to the reduction of the surface oxygen far away from Pt particles and the reduction of subsurface oxygen[27]. The third peak around 680 ℃ observed in all the samples may be ascribed to the reduction of surface $A1^{3+}$ on $\gamma$-$Al_2O_3$[28].

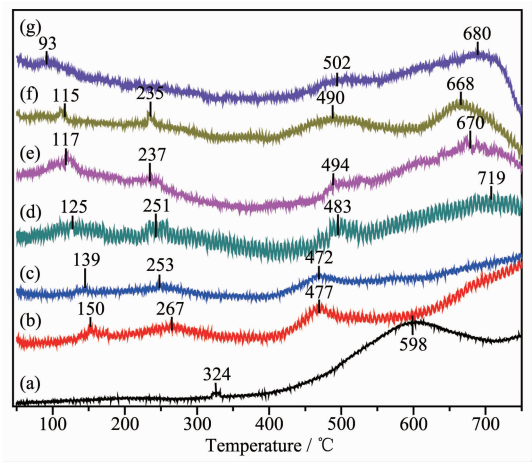


(a) $Au/Al_2O_3$, (b) $Au_3Pt_1/Al_2O_3$, (c) $Au_2Pt_1/Al_2O_3$, (d) $Au_1Pt_1/Al_2O_3$, (e) $Au_1Pt_2/Al_2O_3$, (f) $Au_1Pt_3/Al_2O_3$, (g) $Pt/Al_2O_3$

Fig.4　$H_2$-TPR profiles of Au@Pt catalysts

For bimetallic Au@Pt catalyst, the reduction peak between 115 and 150 ℃ is attributed to the reduction of $PtO_x$, and the reduction peak between 235 and 275 ℃ belongs to the reduction of $Au_xO_y$. In the high temperature (477 ~490 ℃), the reduction peak was basically similar to metal Pt. Because the amount of metal oxides in the catalyst account for a small part, which is in line with the results of XPS, various reduction peaks were weak. In addition, the reduction peaks in the low-temperature region gradually shifted to lower temperatures as the Pt content increased, showing Au and Pt mutually exerts positive influence on their respective reductions. In particular, both $Au_1@Pt_2$ and $Au_1@Pt_3$ reduction peaks were slightly lower than other bimetallic catalysts, indicating the surface oxygen species has a faster migration rate and oxygen vacancies are easier to generate. The position of the reduction peak of the bimetallic Au@Pt catalyst depends on the degree of interaction between Au and Pt. These results demonstrate that there is a strong interaction between Au, Pt and support[29], which improves catalytic activity.

The Pt4*f* and Au4*f* orbital XPS spectra of Au@Pt catalysts are shown in Fig.5. Because the Al2*p* peak overlapped with the Pt4*f* peak in a range of 68 ~80 eV, it is necessary to separate the Al2*p* peak from the spectra. For $Pt/Al_2O_3$, when the Al2*p* was used at 73.9 eV, the Pt4$f_{7/2}$ spectra can be deconvoluted into two peaks at 70.1 and 71.0 eV, and the Pt4$f_{5/2}$ spectra can be also divided into two peaks at 73.4 and 74.3 eV, corresponding to $Pt^0$ and $Pt^{2+}$[30], respectively. In bimetallic system, the Al2*p* needed to be separated from Pt4*f*. The Pt4*f* and Au4*f* fine spectra of bimetallic Au@Pt can be fitted into two sets of peaks, corresponding to the 4$f_{7/2}$ and 4$f_{5/2}$ orbitals of $Pt^0$ and $Pt^{2+}$, $Au^0$ and $Au^{\delta+}$, respectively. The binding energy of Au shifted slightly to lower value (Fig.5B), and the binding energy of Pt increased (Fig.5A) compared to pure Au and Pt with the increase of Pt content, which demonstrates that electronic structure has significantly changed in bimetallic Au@Pt catalysts, and the inter- and intra-atomic charges transfers between Au and Pt[31]. In addition, the difference in electronegativity of Au and Pt (2.54 and 2.28) may imply potential electron-withdrawing effect from Au to neighboring Pt[32], which suggests that the oxidation state of Pt shell is affected by the Au core. Table 2 shows the binding energy and relative content of Au4*f* and Pt4*f* for bimetallic Au@Pt catalysts, and it can be seen that the $Au^0$ and $Pt^0$ contents occupy the majority of the catalyst, indicating

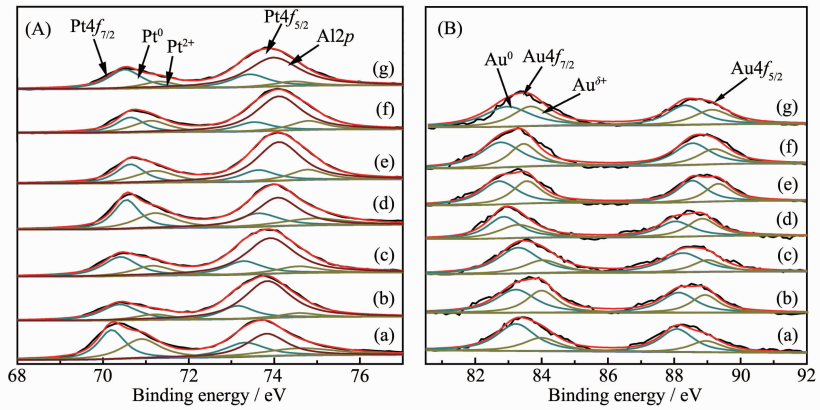


(A-a) $Pt/Al_2O_3$, (B-a) $Au/Al_2O_3$, (b) $Au_3Pt_1/Al_2O_3$, (c) $Au_2Pt_1/Al_2O_3$, (d) $Au_1Pt_1/Al_2O_3$, (e) $Au_1Pt_2/Al_2O_3$, (f) reused $Au_1Pt_2/Al_2O_3$, (g) $Au_1Pt_3/Al_2O_3$

Fig.5 Pt4*f* (A) and Au4*f* (B) XPS spectra of prepared catalysts

**Table 2 Binding energies and proportion of Au4*f* and Pt4*f* of prepared catalyst**

| Catalyst | Binding energy/ eV | | | | Relative proportions/% | |
|---|---|---|---|---|---|---|
| | $Au4f_{7/2}$ | | $Pt4f_{7/2}$ | | | |
| | $Au^0$ | $Au^{\delta+}$ | $Pt^0$ | $Pt^{2+}$ | $Au^0/Au^{\delta+}$ | $Pt^0/Pt^{2+}$ |
| $Au/Al_2O_3$ | 83.38 | 84.20 | — | — | 68/32 | — |
| $Au_3Pt_1/Al_2O_3$ | 83.29 | 84.03 | 70.39 | 71.10 | 58/42 | 74/26 |
| $Au_2Pt_1/Al_2O_3$ | 83.25 | 83.97 | 70.41 | 71.16 | 69/31 | 64/36 |
| $Au_1Pt_1/Al_2O_3$ | 82.85 | 83.56 | 70.55 | 71.23 | 58/42 | 55/45 |
| $Au_1Pt_2/Al_2O_3$ | 82.72 | 83.55 | 70.60 | 71.25 | 57/43 | 53/47 |
| $Au_1Pt_3/Al_2O_3$ | 82.70 | 83.52 | 70.61 | 71.32 | 57/43 | 74/26 |
| $Pt/Al_2O_3$ | — | — | 70.20 | 70.90 | — | 59/41 |
| $Au_1Pt_2/Al_2O_3$ reused | 82.80 | 83.49 | 70.53 | 71.19 | 53/47 | 51/49 |

that $Au^0$ and $Pt^0$ are the main active species on the catalyst surface. According to the XPS data of $Au_1@Pt_2$ after the reaction, the $Au^0/Au^{\delta+}$ and $Pt^0/Pt^{2+}$ proportion were slightly lower than that before the reaction, indicating that the number of main active centers with $Au^0$ and $Pt^0$ decrease as the reaction proceeds. However, the range of variation is small, which indicates that the catalyst has good stability and conforms to the characterization results of XRD and TEM. So the modified electronic structure and active species would improve their catalytic properties.

## 2.4 Catalytic activity of Au@Pt catalysts for toluene oxidation

Fig.6 shows catalytic oxidation of toluene by Au@Pt catalysts prepared with different molar ratios of Au and Pt. In the reaction, the products were only $CO_2$ and water, and CO and other organic small molecules were not detected. The catalytic activity for 98% oxidation of toluene were given in the order of $Au_1Pt_2 \geqslant Au_1Pt_3 > Au_1Pt_1 > Au_2Pt_1 > Au_3Pt_1 > Pt > Au$. And the $T_{98}$ corresponding to the above-mentioned sequential catalyst is 195, 195, 210, 215, 230, 230 and 270 ℃, respectively. However, the $Au_1Pt_2$ catalyst exhibited excellent catalytic activity, which might be due to that

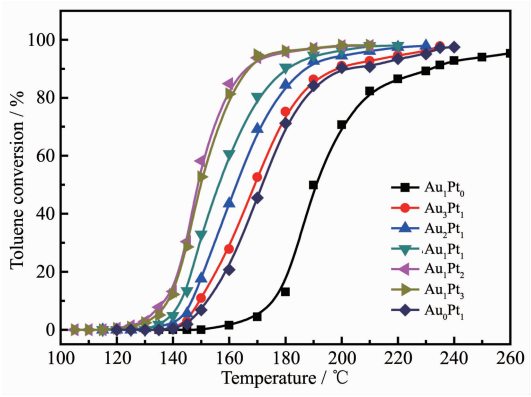


VOC concentration: $1\times10^{-3}$ (*V*/*V*), GHSV of toluene: 18 $L\cdot g^{-1}\cdot h^{-1}$

Fig.6 Catalytic oxidation of toluene with by Au@Pt catalysts prepared with different molar ratios of Au and Pt

it has smaller particle size and better dispersibility. And it also illustrates that the coexistence of Au and Pt in the bimetallic $Au_1Pt_2$ catalyst has higher activity for toluene oxidation compared with monometallic Au or Pt.

### 2.5 Catalyst stability test

To examine the stability of Au, Pt and $Au_1@Pt_2$ catalysts and maintain the reaction temperature at their respective $T_{98}$ under GHSV at 18 $L\cdot g^{-1}\cdot h^{-1}$ with $1\times10^{-3}$ ($V/V$) toluene, the catalysts were taken at regular intervals and analyzed on-line. Fig.7 shows the relationship between toluene conversion, selectivity of carbon dioxide and reaction time. It could be seen that the removal rate of toluene is over 98% and the selectivity of $CO_2$ is 100% within 0~50 h, which indicates the catalysts have high stability and selectivity.

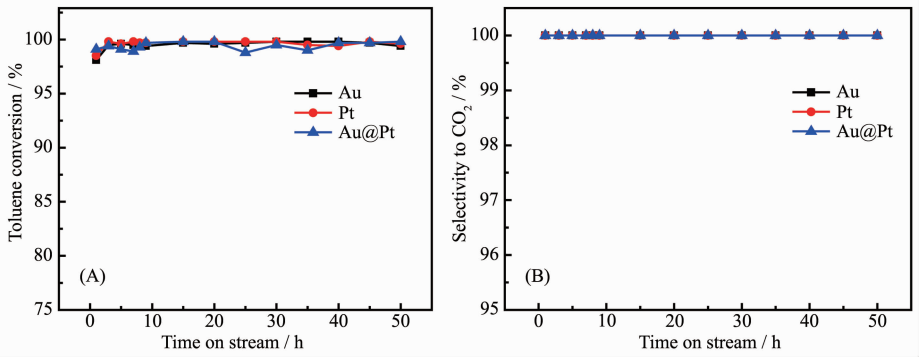


Fig.7　Stability test of toluene oxidation (A) and selectivity to $CO_2$ (B) with time-on-stream over $Au/Al_2O_3$, $Pt/Al_2O_3$, $Au_1@Pt_2/Al_2O_3$ catalysts

In order to examine the effect of water vapor over the $Au_1@Pt_2/Al_2O_3$ catalytic activity, we performed toluene oxidation in the presence of water vapor (volume fraction: 5.0%) over the $Au_1@Pt_2/Al_2O_3$ and the result is shown in Fig.8. The results showed that the addition of water vapor decreased the toluene conversion by 9%. When the water vapor was cut off, the toluene conversion rate gradually increased. This phenomenon indicates that there is strong competitive adsorption on the surface of the catalyst in the three components of water vapor, toluene and oxygen[33].

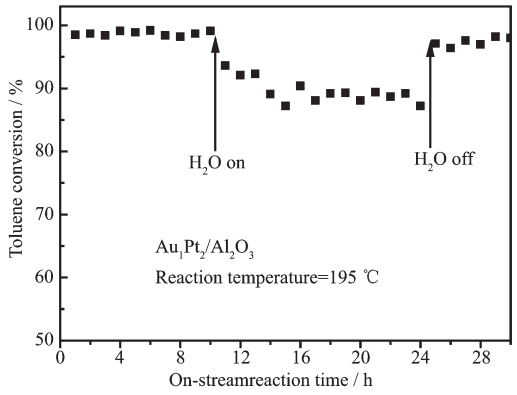


Toluene concentration=$1\times10^{-3}$ ($V/V$), Water vapor concentration= 5.0% ($V/V$), GHSV=18 $L\cdot g^{-1}\cdot h^{-1}$

Fig.8　Effect of water vapor on toluene conversion over $Au_1Pt_2/Al_2O_3$ catalyst

## 3 Conclusions

In summary, the bimetallic Au@Pt core-shell nanoparticles prepared by two-step reduction method have been loaded on the surface of $Al_2O_3$ in a highly dispersed state. The Au@Pt core-shell structure prepared by this method is not only simple but also controllable, which showed higher activity than monometallic Pt or Au catalyst for the oxidation of toluene. The catalytic activity for toluene was given in the order of $Au_1Pt_2 \geqslant Au_1Pt_3 > Au_1Pt_1 > Au_2Pt_1 > Au_3Pt_1 > Pt > Au$. Among the catalysts, the $Au_1@Pt_2/Al_2O_3$ exhibited higher catalytic activity ($T_{98}$=195 ℃) and better stability. These results suggest that the enhancement effect of Au may arise from the electron transfer from Au to Pt, thereby increasing the reactive oxygen species on the surface of Pt. The core-shell structure may find potential applications in the catalytic combustion of VOCs.

Supporting information is available at http://www.wjhxxb.cn

## References:


[1] Salar-García M J, Ortiz-Martínez V M, Hernández-Fernández F J, et al. *J. Hazard. Mater.*, **2017**,**321**:484-499

[2] Scirè S, Liotta L F. *Appl. Catal. B*: *Environ.*, **2012**,**125**:222-246

[3] Kamal M S, Razzak S A, Hossain M M. *Atmos. Environ.*, **2016**,**140**:117-134

[4] Huang H, Xu Y, Feng Q. *Catal. Sci. Technol.*, **2015**,**5**:2649-2669

[5] Zhang Z X, Jiang Z, Weng F S. *Catal. Today*, **2016**,**264**:270-278

[6] Son Y S. *Chem. Eng. J.*, **2017**,**316**:609-622

[7] Finocchio E, Busca G, Notaro M. *Appl. Catal. B*: *Environ.*, **2006**,**62**:12-20

[8] Wang A Q, Liu X Y, Mou C Y, et al. *J. Catal.*, **2013**,**308**:258-271

[9] Zhang Y L, Li X K, Li K, et al. *ACS Appl. Mater. Interfaces*, **2017**,**38**:3268832697

[10]Jeong H, Kim J. *Electrochim. Acta*, **2018**,**283**:11-17

[11]Fedorczyk A, Pomorski R, Chmielewski M, et al. *Electrochim. Acta*, **2017**,**246**:1029-1041

[12]LIU Xiao-Yu(刘晓宇), ZHANG Dong-Jie(张东杰), ZHANG Hui-Juan(张慧娟), et al. *Chinese J. Inorg. Chem.*(无机化学学报), **2018**,**34**:712-718

[13]Xu H, Yan B, Li S M, et al. *Chem. Eng. J.*, **2018**,**334**:2638-2646

[14]Guo S J, Fang Y X, Dong S J, et al. *J. Phys. Chem. C*, **200**, **111**:17104-17109

[15]Park H Y, Park J H, Kim P, et al. *Appl. Catal. B*: *Environ.*, **2017**,**225**:84-90

[16]LI Jia-Heng(李加衡), AO Ping(敖平), LI Xiao-Qing(李小青), et al. *Acta Phys.-Chim. Sin.*(物理化学学报), **2015**,**31**:173-180

[17]Kristian N, Wang X. *Electrochem. Commun.*, **2008**,**10**:12-15

[18]Cao R B, Xia T T, Zhu R Z, et al. *Appl. Surf. Sci.*, **2018**, **433**:840-846

[19]Kang S W, Lee Y W, Park Y S, et al. *ACS Nano*, **2013**,**7**:7945-7955

[20]Guo S J, Li J, Dong S J, et al. *J. Phys. Chem. C*, **2010**,**114**:15337-15342

[21]Liao M Y, Li W P, Xi X P, et al. *J. Electroanal. Chem.*, **2017**,**791**:124-130

[22]Fedorczyk A, Pomorski R, Chmielewski M, et al. *Electrochim. Acta*, **2017**,**246**:1029-1041

[23]Peng R S, Sun X B, Li S J, et al. *Chem. Eng. J.*, **2016**,**306**:1234-1246

[24]Jin B F, Wei Y C, Zhao Z, et al. *Chin. J. Catal.*, **2016**,**37**:923-933

[25]Wei Y C, Liu J, Zhao Z, et al. *J. Catal.*, **2012**,**287**:13-29

[26]Chang C K, Chen Y J, Yeh C T. *Appl. Catal. A*: *Gen.*, **1998**, **174**:13-23

[27]Peng R S, Sun X B, Li S J, et al. *Chem. Eng. J.*, **2016**,**306**:1234-1246

[28]Jia J F, Shen J Y, Lin L W, et al. *J. Mol. Catal. A*: *Chem.*, **1999**,**138**:177-184

[29]Kim K J, Boo S I, Ahn H G. *J. Ind. Eng. Chem.*, **2009**,**15**:92-97

[30]Chen C Y, Zhu J, Chen F, et al. *Appl. Catal. B*: *Environ.*, **2013**,**140**:199-205

[31]Wang R, Wang A J, Liu W D, et al. *Biosens. Bioelectron.*, **2017**,**102**:276-281

[32]Feng R J, Li M, Liu J X. *Colloids Surf. A*, **2012**,**406**:6-12

[33]Yang H G, Deng J G, Xie H H. *Appl. Catal. A*: *Gen.*, **2015**, **507**:139-148